

# Varifocal zoom imaging with large area focal length adjustable metalenses

SHANE COLBURN,<sup>1</sup> ALAN ZHAN,<sup>2</sup> AND ARKA MAJUMDAR<sup>1,2,\*</sup> 

<sup>1</sup>Department of Electrical Engineering, University of Washington, Seattle, Washington 98195, USA

<sup>2</sup>Department of Physics, University of Washington, Seattle, Washington 98195, USA

\*Corresponding author: arka@uw.edu

Received 18 April 2018; revised 12 June 2018; accepted 13 June 2018 (Doc. ID 328732); published 10 July 2018

Varifocal lenses are essential components of dynamic optical systems with applications in photography, mixed reality, and microscopy. Metasurface optics has strong potential for creating tunable flat optics. Existing tunable metalenses, however, typically require microelectromechanical actuators, which cannot be scaled to large area devices, or rely on high voltages to stretch a flexible substrate and achieve a sufficient tuning range. Here, we build a 1 cm aperture varifocal metalens system at 1550 nm wavelength inspired by an Alvarez lens, fabricated using high-throughput stepper photolithography. We demonstrate a nonlinear change in focal length by minimally actuating two cubic phase metasurfaces laterally, with focusing efficiency as high as 57% and a wide focal length change of more than 6 cm (>200%). We also test a lens design at visible wavelength and conduct varifocal zoom imaging with a demonstrated 4× zoom capability without any other optical elements in the imaging path. © 2018 Optical Society of America under the terms of the [OSA Open Access Publishing Agreement](#)

**OCIS codes:** (050.6624) Subwavelength structures; (220.1000) Aberration compensation; (220.4241) Nanostructure fabrication; (160.3918) Metamaterials.

<https://doi.org/10.1364/OPTICA.5.000825>

## 1. INTRODUCTION

Metasurfaces have fostered substantial interest in the optics and photonics communities in recent years. These ultrathin elements comprise arrays of subwavelength-spaced optical antennas that can apply spatially varying transfer functions on incident wavefronts [1–4], including those of lenses [5–11], holograms [12,13], polarization elements [14], vortex beam generators [14–19], and blazed gratings [20,21]. By changing only the lateral geometry and orientation of these optical antennas, the local transmission or reflection coefficient of a metasurface can be tailored for specific applications. Most demonstrated metasurface devices to date, however, have been static in nature. For metalenses, focal length tuning over a wide range is of substantial interest in photography, microscopy, mixed reality, and optical communications. Stretching of metalenses on flexible substrates [22–25] is one route to accomplish this, but this entails constant application of an external force to counteract the substrate's restoring force. Furthermore, electrical control of such systems requires high voltages (kV range), as the tuning mechanism relies on a capacitive electrostatic force to compress an elastomer [25]. Microelectromechanical systems (MEMS)-based tuning is promising, with recent results adjusting the angular orientation of a metalens [26] or demonstrating large changes in optical power by actuating a metalens axially in a compound lens system [27]. Unfortunately, although MEMS devices are quite effective at short length scales, their electrostatic actuation mechanisms

cannot be scaled to the macroscale sizes [28,29] necessary for applications requiring large apertures and focal lengths, such as for eyeglasses and mixed reality displays [30,31]. For large area devices with correspondingly higher tuning ranges and a more massive system, a larger gap distance and actuation is required. With the increased mass and actuation distance, however, the required forces can become too large for electrostatic MEMS devices. As the applied force is proportional to the derivative of the capacitance, with the increased gap, the decrease in capacitance must be compensated for by an increase in voltage [32]. With centimeter-scale devices, the voltage required to induce sufficient displacement of large area metalenses would cause electrical breakdown and device failure [28,29,32].

Here, we develop a large area tunable focal length metalens system using an Alvarez lens design [33,34], combining two separate cubic metasurfaces that under lateral actuation give rise to a rapid and nonlinear change in focal length [Fig. 1(a)]. Unlike most previous metasurface works, we fabricate our device using high-throughput stepper photolithography, circumventing the scalability issues of electron-beam lithography to build a large area (1 cm<sup>2</sup> aperture) device. Our process flow relies on a custom-developed compression algorithm that can substantially reduce the complexity of layout files, enabling us to create a metalens with nearly 120 million scatterers with, to the best of our knowledge, the largest focal length range demonstrated to date. We use a versatile silicon nitride cylindrical nanopost platform, which is

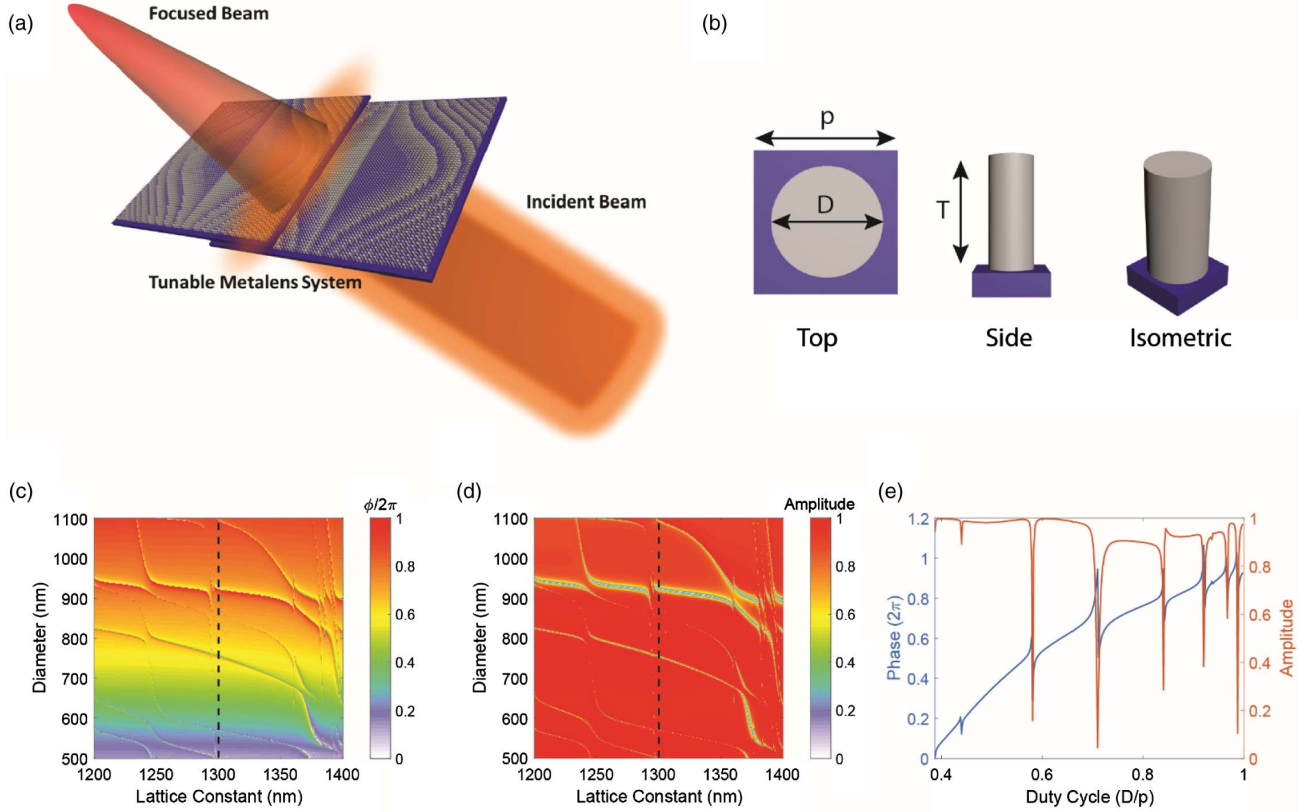


**Fig. 1.** Simulation and design of nanoposts: (a) Schematic representation of our tunable metalens system comprising two cubic metasurface phase plates actuated laterally. (b) Top, side, and isometric views of our silicon nitride nanoposts where  $T$  is thickness,  $D$  is diameter, and  $p$  is lattice constant. The simulated amplitude (c) and phase (d) of the transmission coefficient as a function of nanopost diameter and lattice constant are shown. (e) Phase and amplitude for a fixed lattice constant of  $1.3 \mu\text{m}$  corresponding to the black dashed lines in (c) and (d).

polarization insensitive and well suited for efficient operation from the visible to the infrared. In this work, our Alvarez metalens is actuated manually using translation stages; however, electrical actuation is well within the means of commercially available miniature stepper motors [35]. We propose this actuator mechanism for the case of large area metalenses, maintaining that such a mechanism is not well suited for microscale structures, where MEMS-based actuators are effective. With the wide aperture of our system, we demonstrate its utility for varifocal zoom imaging without requiring any additional elements (e.g., objectives or tube lenses) in the optical path, achieving a magnification range with  $4\times$  zoom capability in our experiments.

## 2. DESIGN

### A. Theory and Simulation

The phase profile of a spherical singlet metalens follows a quadratic form that is inversely proportional to its focal length. An Alvarez lens instead comprises two separate cubic phase plates that in conjunction give rise to a tunable focal length lens when the plates are actuated laterally with respect to one another. These phase plates are typically implemented using freeform glass surfaces or multi-level diffractive optics, entailing sophisticated and expensive fabrication. For our design, we use two flat metasurface phase plates, where one plate obeys a cubic polynomial function and the other follows the same function but with opposite sign. When the plates are aligned along the optical axis and positioned

parallel to one another, under lateral actuation, the total phase profile imparted on an incident wavefront is a quadratic function with changing focus. The phase profiles of the regular and inverse metasurfaces are

$$\varphi_{\text{reg}}(x, y) = -\varphi_{\text{inv}}(x, y) = A \left( \frac{1}{3}x^3 + xy^2 \right), \quad (1)$$

where  $A$  is a constant with units of inverse cubic length and  $(x, y)$  represents the in-plane position. The constant  $A$  denotes the cubic phase strength and is equal to  $\frac{2\pi\alpha}{L^3}$ , where  $L$  is half the aperture width, and  $\alpha$  gives the number of  $2\pi$  cycles exhibited in traversing a path along the  $x$  axis from the origin to the edge of the aperture of the cubic mask. Translating these phase masks by a displacement  $d$  in opposite directions, we obtain a quadratic form as below:

$$\begin{aligned} \varphi_{\text{Alvarez}}(x, y) &= \varphi_{\text{reg}}(x + d, y) + \varphi_{\text{inv}}(x - d, y) \\ &= 2Ad(x^2 + y^2) + \frac{2}{3}Ad^3. \end{aligned} \quad (2)$$

Neglecting the constant  $d^3$  phase term and relating the quadratic term to the phase of a spherical singlet, we find the focal length as a function of displacement as

$$f(d) = \frac{\pi}{2\lambda Ad}, \quad (3)$$

where  $f$  is the focal length and  $\lambda$  is the wavelength. The inverse dependence of the focal length on the displacement  $d$  induces a

nonlinear and rapid change in focal length for small displacements. For a design wavelength of 1550 nm we select the value  $A = 6.756 \times 10^9 \text{ m}^{-3}$  such that, by changing  $d$  from 1 mm to 4 mm, we can tune the focal length continuously from 3.75 cm to 15 cm.

To implement our tunable lens, we need to design dielectric scatterers capable of supporting high-efficiency operation while remaining compatible with the spatial resolution achievable with photolithography. For the designed focal length, a large aperture is required to cover the necessary actuation range and achieve a numerical aperture (NA) high enough to image with sufficient resolution. While large area metalenses with moderate to high NA do exist, these devices rely on expensive and time-consuming electron-beam lithography, precluding widespread commercial adoption. Recently, mass manufacturing-compatible large area metalenses at 1550 nm were reported [36]. Our process flow is similar to this work [36]; however, we use a silicon nitride nanopost platform and demonstrate devices on both silicon and quartz substrates, enabling visible wavelength operation in addition to 1550 nm. While our selection of silicon nitride as the nanopost material limits beam deflection efficiency at high angles [37] and focusing efficiency at high NAs [38] relative to state-of-the-art high-index silicon-based metalenses, the platform is advantageous in providing lossless operation over a broad wavelength range, unlike silicon devices that absorb significantly at visible wavelengths. Depending on the application and wavelength of interest, our design process can be adapted to different nanopost materials, contingent on whether absorption or diffraction efficiency at high angles is of higher priority.

To work within the constraints of our university cleanroom's stepper lithography system, we limited the minimum diameter of our silicon nitride cylindrical nanoposts [Fig. 1(b)] to 500 nm and designed scatterers using rigorous coupled-wave analysis (RCWA) [39]. Figure 1(e) shows the simulated transmission coefficient at 1550 nm of our designed 2  $\mu\text{m}$  thick silicon nitride nanoposts on a silicon substrate. We use a lattice spacing of 1.3  $\mu\text{m}$  and have diameters ranging from 500 nm to 1.1  $\mu\text{m}$ . As evidenced by the minimal variation in transmission coefficient over a wide range of lattice periodicities [Figs. 1(c)–1(d)], we can approximate our nanoposts as weakly coupled dielectric scatterers, justifying our subsequent use of the unit cell approximation in designing the metasurface [8]. These nanoposts can be understood as behaving like truncated circular waveguides in which the discontinuities in refractive index at the top and bottom interfaces of the scatterers produce Fresnel reflections and low-quality factor Fabry–Perot resonances. Together these modes produce the nanoposts' complex transmission coefficient. The transmission coefficient in Fig. 1(e) exhibits multiple resonances, which we attribute to guided mode resonances (GMRs) arising from coupling of incident radiation to surface modes in the grating layer. The electromagnetic power of GMRs is strongly confined within the grating layer but can still couple to free space [40,41]. Near the post diameters exhibiting GMRs, the phase varies rapidly, and the amplitude drops significantly, but as we select diameters off resonance when designing our metasurfaces, these changes in amplitude do not impact our efficiency. GMRs are extensively studied in photonic crystal slabs and metasurfaces, and they can be eliminated by ensuring the phase-matching condition is not satisfied [40–43]. To break this condition, the center-to-center distance of the nanoposts needs to be reduced to less

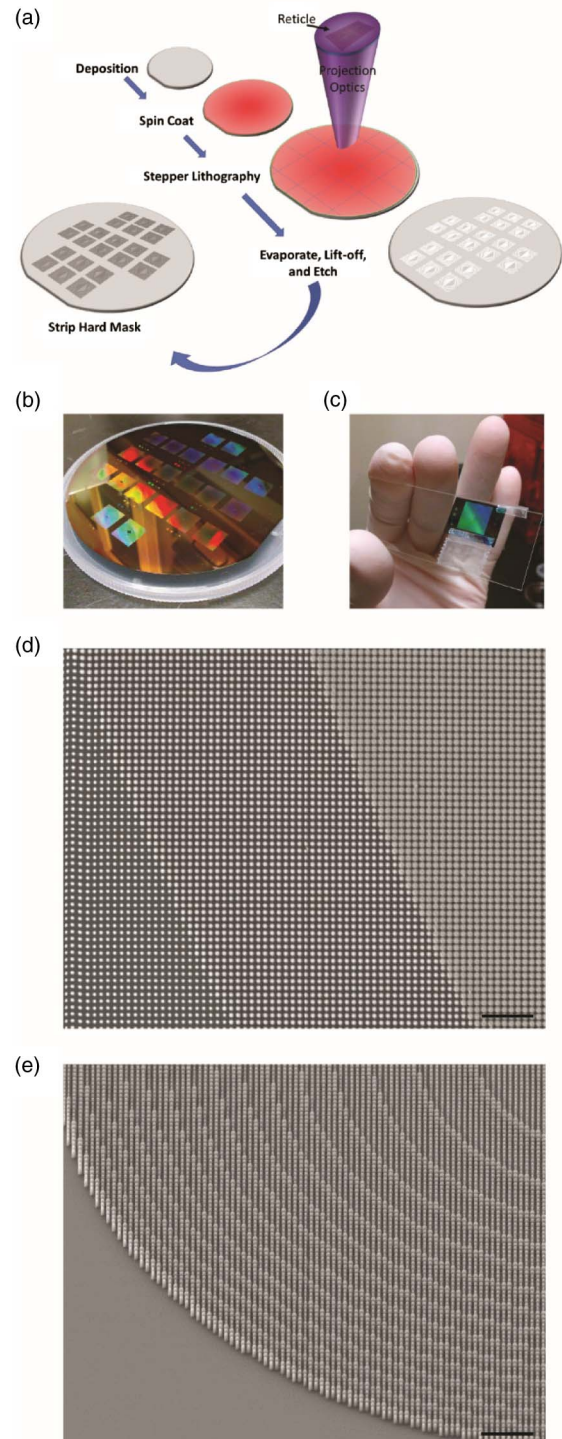


**Fig. 2.** Fabrication of the large area metasurfaces. (a) Schematic of the process flow for fabricating multiple large area metalenses in parallel using high-throughput stepper lithography-based processing. (b) Fully exposed and developed 100 mm wafer, showing the capability to make large area devices. (c) A fully etched and cleaved metasurface cubic phase plate with a hand for scale. Scanning electron micrographs of fabricated nanoposts are shown at (d) normal incidence and (e) 45° incidence. Scale bars 10  $\mu\text{m}$ .

than the effective wavelength inside silicon nitride, which is feasible using state-of-the-art deep UV stepper lithography systems.

## B. Fabrication

To make our metasurface cubic phase plates, we used the calculated transmission coefficient data as a lookup table, mapping the desired phase to the corresponding nanopost diameter. Fabricating the desired metasurfaces required manufacturing a reticle in accordance with a layout file, such as a GDSII, detailing the positions and diameters of nearly 120 million nanoposts. Whereas layout files for typical metasurface designs usually contain individual cells for each nanopost due to the small number of individual posts, for the exceedingly large number of elements in our design, we had to develop an algorithm (see Supplement 1, Section S5) based on hierarchical cell references to reduce the required memory. Minimizing the memory is critical, as layout files must undergo computationally demanding processing, such as fracturing, to convert the data into the proper format for manufacturing a reticle. With the number of elements increasing quadratically with a linear increase in aperture width, layout file compression is crucial to be able to support large area metalenses. By writing our layout file using our algorithm and converting to an OASIS file, we achieved more than a 2600 $\times$  reduction in memory. While a previously developed metasurface layout file compression algorithm [36] showed an even larger reduction, our algorithm is more general in that it does not require any symmetry in the layout and can be used for general phase masks such as those for holograms or our cubic surfaces.

Figure 2(a) schematically summarizes our fabrication process flow, including deposition, spin coating, stepper lithography, hard mask patterning and etching, and mask removal. Figures 2(b) and 2(c) show a standard 100 mm wafer after our exposure step and an etched and cleaved cubic metasurface phase plate with a hand for scale, respectively. In Figs. 2(d) and 2(e), we can see scanning electron micrographs of the fabricated nanoposts from normal and diagonal (45 $^\circ$ ) views, respectively. In addition to the designed metasurface Alvarez lens, our reticle also included several static singlet and vortex beam-generating metalenses to demonstrate the versatility of our nanopost design and fabrication process. In characterizing these devices, we saw close to diffraction-limited performance and successful generation of vortex beams with different orbital angular momentum states (see Supplement 1, Section S2 and Fig. S1).

## 3. EXPERIMENTAL RESULTS

We experimentally verified the tunable behavior of our Alvarez metalens system by laterally displacing the regular and inverse cubic metasurfaces with respect to one another (see Supplement 1, Section S3 and Fig. S2(a) for a schematic and description of the measurement setup). We displaced the metasurfaces over a 2.75 mm range, translating to a nonlinear change in focal length over a 6.62 cm range at 1550 nm, matching closely with the theoretical focal length [Fig. 3(a)]. With the same reticle layout, we also fabricated a lens on a quartz substrate to operate at 633 nm wavelength. While this visible regime device is not strictly a metasurface due to its super-wavelength lattice periodicity, the near-wavelength spacing still enables a wide range of phase shifts as a function of diameter, even with fixed nanopost thickness [Fig. 3(b)]. For this simulation, the nanoposts have the same lattice constant as before, but we use a lower thickness of 1.5  $\mu\text{m}$ ,

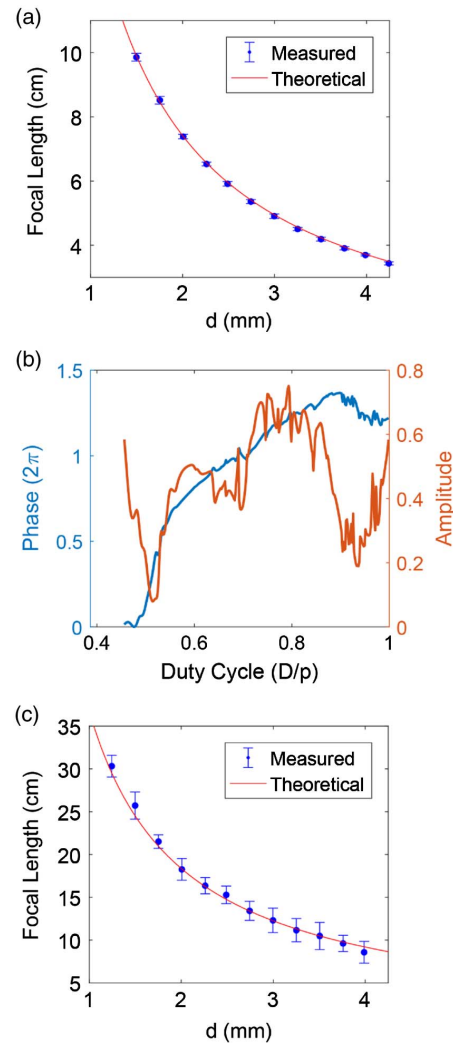


**Fig. 3.** Experimental and theoretical focal lengths of the tunable lens designs. Focal lengths as a function of lateral displacement for the infrared (a) and visible (c) designs are shown. Errors bars represent a 95% confidence interval where the  $1\sigma$  uncertainty is estimated during measurement by finding the range of distances over which the lens appears to be in focus. (b) Simulated transmission coefficient of the 1.5  $\mu\text{m}$  thick silicon nitride nanoposts on a quartz substrate.

which exhibited higher transmission amplitude. In having the same spatial arrangement of nanopost positions and diameters by using the same reticle as for the silicon substrate design, the metalens will still focus; however, as chromatic aberrations in metasurfaces are primarily a result of phase-wrapping discontinuities [44], in illuminating at 633 nm, the phase function will exhibit discontinuities that will induce a chromatic focal shift. The resultant focal length of the metalens on quartz can be estimated via Eq. (3), and the strong agreement of this theoretical focal length and the experimentally measured focusing (see Supplement 1, Section S3 and Fig. S2(b) for a schematic and description of the measurement setup) confirms this behavior [Fig. 3(c)].

The visible lens design with its super-wavelength lattice constant does, however, come at the cost of producing higher diffraction orders that are absent for devices on a subwavelength lattice. The 1550 nm and 633 nm designs achieved focusing

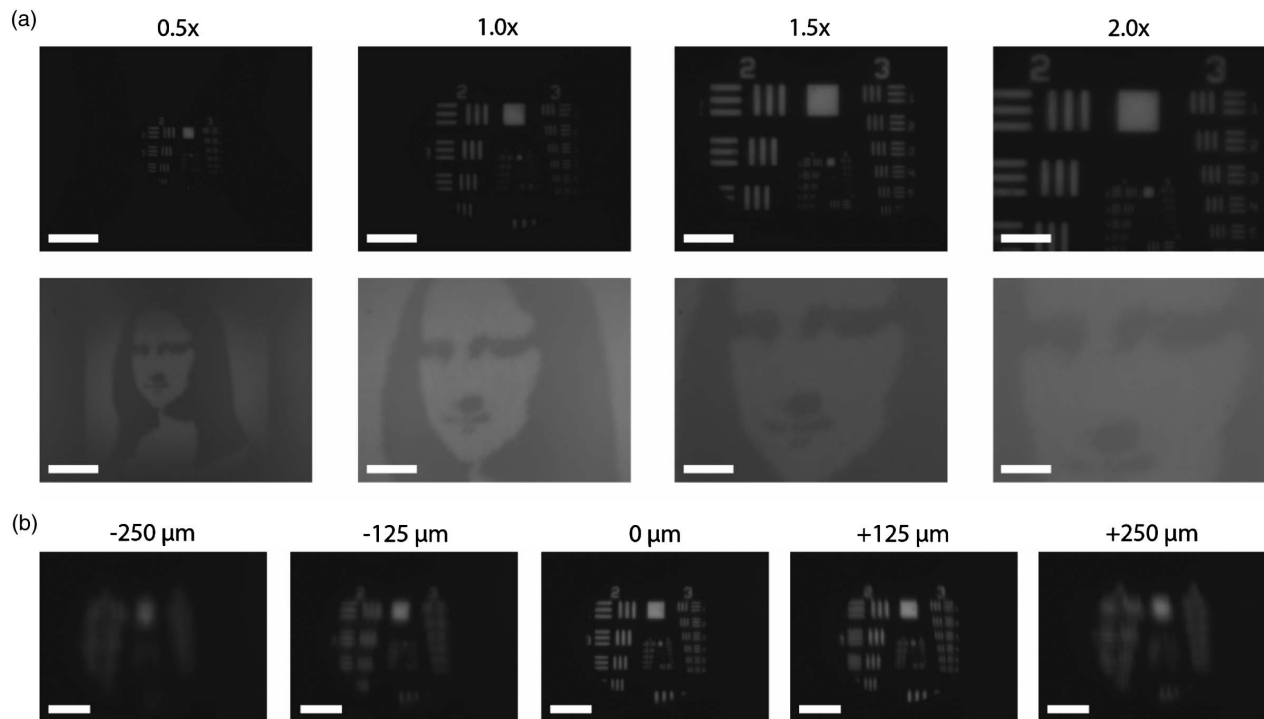


**Fig. 4.** Imaging with different magnifications using the visible lens design. (a) Examples of images captured without any optical elements aside from the tunable lens system in the optical path using an Air Force resolution test chart illuminated in transmission (top row) and a Mona Lisa pattern printed on paper illuminated by scattering light off the pattern (bottom row). (b) Effect of misaligning the regular cubic metasurface phase plate on image quality. The scale bar is 1.2 mm for all images.

efficiencies of 57% and 15%, respectively, at a displacement  $d$  of 2.5 mm. The large efficiency drop at 633 nm is attributed to light being lost to these additional diffraction orders, and when considering the focusing efficiency of the zeroth order beam alone (i.e., neglecting light lost to higher order diffraction, see Supplement 1, Section S1 for details), we achieve an efficiency of 58%, close to that of the 1550 nm device. We note that our university cleanroom sets a lower limit on our achievable lattice constant, but subwavelength lattices for visible frequencies are well within the capabilities of state-of-the-art deep-UV lithography systems (see Supplement 1, Section S7 and Fig. S4 for a nanopost design compatible with such systems). With a subwavelength lattice constant, we could suppress these higher diffraction orders and increase the efficiency of the 633 nm design. As calculated via angular spectrum propagation [45], the theoretical focusing efficiency of our 1550 nm lens is 92%, indicating a significant drop in performance arising from fabrication imperfections, likely resulting from overexposure of the nanoposts during

the lithography stage. Furthermore, we also attribute this drop to the fact that our system comprises two optical elements, where it is assumed that light is normally incident on all scatterers in RCWA, but for our second cubic phase plate, the incident wavefront consists of oblique wavevectors after being diffracted by the first plate. This alters the scattering properties of the nanoposts and prevents exact implementation of the desired phase profile.

Our widely focus-tunable lens is well suited for imaging with different values of magnification for varifocal zoom applications. To examine the imaging performance of our device, we illuminated a 1951 Air Force resolution test chart with a 625 nm LED in transmission and imaged the pattern directly onto a camera with our tunable lens on a quartz substrate without the use of supplemental optics (see Supplement 1, Section S4 and Fig. S3(a) for a schematic and description of the measurement setup). By fixing the test chart 30 cm away and tuning the focal length from 10 cm to 20 cm (1.8 mm actuation of each metasurface) and appropriately shifting the camera to the image plane, we provided magnifications

**Table 1. Comparison among Different Existing Mechanically Tunable Metalens Systems**

| Reference                 | Actuation Mechanism             | Focal Length Change (cm) | Optical Power Change ( $\text{m}^{-1}$ ) | Wavelength (nm) | Polarization |
|---------------------------|---------------------------------|--------------------------|--|-----------------|--------------|
| Ee <i>et al.</i> [23]     | Stretching                      | $1 \times 10^{-2}$       | 2667                                     | 633             | Circular     |
| Kamali <i>et al.</i> [24] | Stretching                      | $8 \times 10^{-2}$       | 952                                      | 915             | Insensitive  |
| She <i>et al.</i> [25]    | Stretching (electrical control) | 1.5                      | 5  | 1550            | Insensitive  |
| Arbabi <i>et al.</i> [27] | MEMS                            | $6.4 \times 10^{-3}$     | 180                                      | 915             | Insensitive  |
| Zhan <i>et al.</i> [34]   | Alvarez                         | 0.25                     | 1600                                     | 633             | Insensitive  |
| This work                 | Alvarez                         | 6.62                     | 21                                       | 1550            | Insensitive  |
| This work                 | Alvarez                         | 32.4                     | 9  | 633             | Insensitive  |

ranging from  $0.5\times$  to  $2\times$ , achieving a  $4\times$  zoom range [Fig. 4(a)]. We repeated this measurement for imaging a Mona Lisa pattern prepared on standard printer paper by scattering the LED light off the pattern (see Supplement 1, Section S4 and Fig. S3(b) for a schematic and description of the measurement setup). To demonstrate the narrow actuation range required for changing the optical power of our metalens and its effect on imaging, we varied the degree of lateral misalignment of the two plates over a small range ( $-250\ \mu\text{m}$  to  $+250\ \mu\text{m}$ ) and recorded a video of the Air Force pattern with this actuation in real time (see Visualization 1). Snapshots at specific levels of misalignment are also provided in Fig. 4(b). The narrow range required to actuate the device demonstrates the sensitivity of this tuning method, where the nonlinear change in focal length is very abrupt as a function of displacement. The shifting and blurring of the image pattern in Fig. 4(b) arise from the alteration to the system's phase function, in which the misalignment both longitudinally shifts the focal plane and adds a linear phase ramp that laterally translates the image (see Supplement 1, Section S6 for a derivation of the misaligned phase function).

#### 4. DISCUSSION AND CONCLUSION

Our tunable metalens system demonstrates a large change in optical power (20.8 diopters at 1550 nm and 9.2 diopters at 633 nm) with, to the best of our knowledge, the largest focal length range (6.62 cm at 1550 nm and 32.4 cm at 633 nm, 205% and 378% changes,  $\frac{f_{\text{max}}-f_{\text{min}}}{f_{\text{min}}}$ , respectively) for an optical metasurface demonstrated to date. Table 1 summarizes and compares some of the properties of existing mechanically tunable metalenses with the devices demonstrated in this work, indicating our designs achieved only moderate changes in optical power but very large focal length ranges. This large tuning range is enabled not only by the inverse proportionality between focal length and displacement for Alvarez lenses, but also by our developed stepper lithography platform and silicon nitride nanoposts, which can provide elements with much wider apertures using methods compatible with mass manufacturing. Currently, however, the metasurfaces in our demonstrated device are actuated by hand using micrometer translation stages. Such stages would be incompatible for any portable lens platform. Whereas the wide aperture of our device is one of its primary benefits, the corresponding increased mass of our optical element precludes MEMS-based actuation as demonstrated with other tunable metasurface systems [26,27]. The actuation is, however, well within the capabilities of commercial off-the-shelf stepper motors [35], such as those used to drive small masses or gears in wristwatches. Integration of our large area metasurface cubic phase plates with these actuators would provide rapid and low-power (zero static power dissipation) focal length-tunable metalenses.

The developed tunable lens also demonstrated varifocal zoom imaging, adjusting magnification from  $0.5\times$  to  $2\times$ , with large ( $10$ 's of centimeters) object and image distances. While we did not demonstrate a true parfocal zoom with our device, integration of two such Alvarez lenses [46] would allow for zoom imaging with stationary optical components and fixed object and image positions. Integrating these two separate devices in a compact form factor would require modification of the tunable focal length range and therefore increasing the constant  $A$  in Eq. (3) to provide a design with shorter focal lengths.

The reported system demonstrates metalenses with a wide focal length tuning range and varifocal zoom imaging capability requiring minimal lateral actuation. Expanding on our previous work integrating two cubic metasurfaces [34], this system provides a tunable metalens with nearly 120 million nanoposts, more than 1300 times the number in our previous work, attributable to the stepper photolithography-compatible processing we developed with a versatile nanopost platform. This wide tuning range and varifocal zoom capability could find applications in microscopy, planar cameras, mixed reality, and light detection and ranging (lidar). The demonstrated metalens provides a pathway for metasurfaces to become a viable commercial technology, leveraging existing mass manufacturing processes and commercial off-the-shelf electronics to reduce the mass and volume of optical systems while retaining sufficient imaging quality and providing a low-power tuning mechanism.

**Funding.** Amazon Catalyst; Samsung-GRO.

**Acknowledgment.** This work was facilitated through the use of advanced computational, storage, and networking infrastructure provided by the Hyak supercomputer system at the University of Washington (UW). Part of this work was conducted at the Washington Nanofabrication Facility/Molecular Analysis Facility, a National Nanotechnology Coordinated Infrastructure (NNCI) site at the University of Washington, which is supported in part by funds from the Molecular Engineering & Sciences Institute, the Clean Energy Institute, the Washington Research Foundation, the M. J. Murdock Charitable Trust, the National Science Foundation, and the National Institutes of Health.

See Supplement 1 for supporting content.

#### REFERENCES

1. N. Yu and F. Capasso, "Flat optics with designer metasurfaces," *Nat. Mater.* **13**, 139–150 (2014).
2. A. V. Kildishev, A. Boltasseva, and V. M. Shalaev, "Planar photonics with metasurfaces," *Science* **339**, 1232009 (2013).
3. N. Yu, P. Genevet, M. A. Kats, F. Aieta, J.-P. Tetienne, F. Capasso, and Z. Gaburro, "Light propagation with phase discontinuities: generalized laws of reflection and refraction," *Science* **334**, 333–337 (2011).
4. S. Jahani and Z. Jacob, "All-dielectric metamaterials," *Nat. Nanotechnol.* **11**, 23–36 (2016).
5. A. Arbabi, R. M. Briggs, Y. Horie, M. Bagheri, and A. Faraon, "Efficient dielectric metasurface collimating lenses for mid-infrared quantum cascade lasers," *Opt. Express* **23**, 33310–33317 (2015).
6. P. R. West, J. L. Stewart, A. V. Kildishev, V. M. Shalaev, V. V. Shkunov, F. Strohkendl, Y. A. Zakharenkov, R. K. Dodds, and R. Byren, "All-dielectric subwavelength metasurface focusing lens," *Opt. Express* **22**, 26212–26221 (2014).
7. F. Lu, F. G. Sedgwick, V. Karagodsky, C. Chase, and C. J. Chang-Hasnain, "Planar high-numerical-aperture low-loss focusing reflectors and lenses using subwavelength high contrast gratings," *Opt. Express* **18**, 12606–12614 (2010).
8. A. Arbabi, Y. Horie, A. J. Ball, M. Bagheri, and A. Faraon, "Subwavelength-thick lenses with high numerical apertures and large efficiency based on high-contrast transmitarrays," *Nat. Commun.* **6**, 8069 (2015).
9. D. Lin, P. Fan, E. Hasman, and M. L. Brongersma, "Dielectric gradient metasurface optical elements," *Science* **345**, 298–302 (2014).
10. D. Fattal, J. Li, Z. Peng, M. Fiorentino, and R. G. Beausoleil, "Flat dielectric grating reflectors with focusing abilities," *Nat. Photonics* **4**, 466–470 (2010).
11. F. Aieta, P. Genevet, M. A. Kats, N. Yu, R. Blanchard, Z. Gaburro, and F. Capasso, "Aberration-free ultrathin flat lenses and axicons at telecom

- wavelengths based on plasmonic metasurfaces,” *Nano Lett.* **12**, 4932–4936 (2012).
12. X. Ni, A. V. Kildishev, and V. M. Shalaev, “Metasurface holograms for visible light,” *Nat. Commun.* **4**, 2807 (2013).
  13. G. Zheng, H. Mühlenbernd, M. Kenney, G. Li, T. Zentgraf, and S. Zhang, “Metasurface holograms reaching 80% efficiency,” *Nat. Nanotechnol.* **10**, 308–312 (2015).
  14. A. Arbabi, Y. Horie, M. Bagheri, and A. Faraon, “Dielectric metasurfaces for complete control of phase and polarization with subwavelength spatial resolution and high transmission,” *Nat. Nanotechnol.* **10**, 937–943 (2015).
  15. M. I. Shalaev, J. Sun, A. Tsukernik, A. Pandey, K. Nikolskiy, and N. M. Litchinitser, “High-efficiency all-dielectric metasurfaces for ultracompact beam manipulation in transmission mode,” *Nano Lett.* **15**, 6261–6266 (2015).
  16. K. E. Chong, I. Staude, A. James, J. Dominguez, S. Liu, S. Campione, S. Subramania, T. S. Luk, M. Decker, D. N. Neshev, I. Brener, and Y. S. Kivshar, “Polarization-independent silicon metadevices for efficient optical wavefront control,” *Nano Lett.* **15**, 5369–5374 (2015).
  17. G. Li, M. Kang, S. Chen, S. Zhang, E. Y.-B. Pun, K. W. Cheah, and J. Li, “Spin-enabled plasmonic metasurfaces for manipulating orbital angular momentum of light,” *Nano Lett.* **13**, 4148–4151 (2013).
  18. S. Vo, D. Fattal, W. V. Sorin, Z. Peng, T. Tran, M. Fiorentino, and R. G. Beausoleil, “Sub-wavelength grating lenses with a twist,” *IEEE Photon. Technol. Lett.* **26**, 1375–1378 (2014).
  19. Y. Yang, W. Wang, P. Moitra, I. I. Kravchenko, D. P. Briggs, and J. Valentine, “Dielectric meta-reflectarray for broadband linear polarization conversion and optical vortex generation,” *Nano Lett.* **14**, 1394–1399 (2014).
  20. P. Lalanne, S. Astilean, P. Chavel, E. Cambri, and H. Launois, “Blazed binary subwavelength gratings with efficiencies larger than those of conventional échellette gratings,” *Opt. Lett.* **23**, 1081–1083 (1998).
  21. S. Astilean, P. Lalanne, P. Chavel, E. Cambri, and H. Launois, “High-efficiency subwavelength diffractive element patterned in a high-refractive-index material for 633 nm,” *Opt. Lett.* **23**, 552–554 (1998).
  22. P. Gutruf, C. Zou, W. Withayachumnankul, M. Bhaskaran, S. Sriram, and C. Fumeaux, “Mechanically tunable dielectric resonator metasurfaces at visible frequencies,” *ACS Nano* **10**, 133–141 (2016).
  23. H.-S. Ee and R. Agarwal, “Tunable metasurface and flat optical zoom lens on a stretchable substrate,” *Nano Lett.* **16**, 2818–2823 (2016).
  24. S. M. Kamali, E. Arbabi, A. Arbabi, Y. Horie, and A. Faraon, “Highly tunable elastic dielectric metasurface lenses,” *Laser Photon. Rev.* **10**, 1002–1008 (2016).
  25. A. She, S. Zhang, S. Shian, D. R. Clarke, and F. Capasso, “Adaptive metalenses with simultaneous electrical control of focal length, astigmatism, and shift,” *Sci. Adv.* **4**, eaap9957 (2018).
  26. T. Roy, S. Zhang, I. W. Jung, M. Troccoli, F. Capasso, and D. Lopez, “Dynamic metasurface lens based on MEMS technology,” *APL Photon.* **3**, 021302 (2018).
  27. E. Arbabi, A. Arbabi, S. M. Kamali, Y. Horie, M. Faraji-Dana, and A. Faraon, “MEMS-tunable dielectric metasurface lens,” *Nat. Commun.* **9**, 812 (2018).
  28. I. Shimoyama, “Scaling in microrobots,” in *Proceedings 1995 IEEE/RSJ International Conference on Intelligent Robots and Systems. Human Robot Interaction and Cooperative Robots* (1995), Vol. **2**, pp. 208–211.
  29. R. S. Fearing, “Survey of sticking effects for micro parts handling,” in *Proceedings 1995 IEEE/RSJ International Conference on Intelligent Robots and Systems. Human Robot Interaction and Cooperative Robots* (1995), Vol. **2**, pp. 212–217.
  30. C. Hong, S. Colburn, and A. Majumdar, “Flat metaform near-eye visor,” *Appl. Opt.* **56**, 8822–8827 (2017).
  31. D. Lin, M. Mellii, E. Poliakov, P. S. Hilaire, S. Dhuey, C. Peroz, S. Cabrini, M. Brongersma, and M. Klug, “Optical metasurfaces for high angle steering at visible wavelengths,” *Sci. Rep.* **7**, 2286 (2017).
  32. R. Legtenberg, A. W. Groeneveld, and M. Elwenspoek, “Comb-drive actuators for large displacements,” *J. Micromech. Microeng.* **6**, 320–329 (1996).
  33. L. W. Alvarez, “Two-element variable-power spherical lens,” U.S. patent 3,305,294 (3 December, 1964).
  34. A. Zhan, S. Colburn, C. M. Dodson, and A. Majumdar, “Metasurface free-form nanophotonics,” *Sci. Rep.* **7**, 1673 (2017).
  35. V. V. Athani, *Stepper Motors: Fundamentals, Applications and Design* (New Age International, 1997).
  36. A. She, S. Zhang, S. Shian, D. R. Clarke, and F. Capasso, “Large area metalenses: design, characterization, and mass manufacturing,” *Opt. Express* **26**, 1573–1585 (2018).
  37. J. Yang and J. A. Fan, “Analysis of material selection on dielectric metasurface performance,” *Opt. Express* **25**, 23899–23909 (2017).
  38. E. Bayati, A. Zhan, S. Colburn, and A. Majumdar, “The role of refractive index in metalens performance,” arXiv:1805.04659 (2018).
  39. V. Liu and S. Fan, “S4: a free electromagnetic solver for layered periodic structures,” *Comput. Phys. Commun.* **183**, 2233–2244 (2012).
  40. S. S. Wang and R. Magnusson, “Theory and applications of guided-mode resonance filters,” *Appl. Opt.* **32**, 2606–2613 (1993).
  41. S. Fan and J. D. Joannopoulos, “Analysis of guided resonances in photonic crystal slabs,” *Phys. Rev. B* **65**, 235112 (2002).
  42. M. Khorasaninejad, Z. Shi, A. Y. Zhu, W. T. Chen, V. Sanjeev, A. Zaidi, and F. Capasso, “Achromatic metalens over 60 nm bandwidth in the visible and metalens with reverse chromatic dispersion,” *Nano Lett.* **17**, 1819–1824 (2017).
  43. Z. Shi, M. Khorasaninejad, Y.-W. Huang, C. Roques-Carnes, A. Y. Zhu, W. T. Chen, V. Sanjeev, Z.-W. Ding, M. Tamagnone, K. Chaudhary, R. C. Devlin, C.-W. Qiu, and F. Capasso, “Single-layer metasurface with controllable multiwavelength functions,” *Nano Lett.* **18**, 2420–2427 (2018).
  44. E. Arbabi, A. Arbabi, S. M. Kamali, Y. Horie, and A. Faraon, “Multiwavelength polarization-insensitive lenses based on dielectric metasurfaces with meta-molecules,” *Optica* **3**, 628–633 (2016).
  45. J. W. Goodman, *Introduction to Fourier Optics* (Roberts and Company Publishers, 2005).
  46. J. Schwiegerling and C. Paleta-Toxqui, “Minimal movement zoom lens,” *Appl. Opt.* **48**, 1932–1935 (2009).